Observations of a Filamentous Intrusion and Vigorous Submesoscale Turbulence within a Cyclonic Mesoscale Eddy

ZHENDONG HU,[a] HONGYANG LIN,[a] ZHIYU LIU,[a] ZHIYONG CAO,[a] FANGTAO ZHANG,[a] ZONGPEI JIANG,[b] YAO ZHANG,[a] KUANBO ZHOU,[a] AND MINHAN DAI[a]

[a] *State Key Laboratory of Marine Environmental Science, College of Ocean and Earth Sciences, Xiamen University, Xiamen, China*
[b] *Ocean College, Zhejiang University, Zhoushan, China*

(Manuscript received 13 September 2022, in final form 24 March 2023, accepted 27 March 2023)

ABSTRACT: Oceanic submesoscale flows are considered to be a crucial conduit for the downscale transfer of oceanic mesoscale kinetic energy and upper-ocean material exchange, both laterally and vertically, but defining observations revealing submesoscale dynamics and/or transport properties remain sparse. Here, we report on an elaborate observation of a warm and fresh filament intruding into a cyclonic mesoscale eddy. By integrating cruise measurements, satellite observations, particle-tracking simulations, and the trajectory of a surface drifter, we show that the filament originated from an anticyclonic eddy immediately to the west of the cyclonic eddy, and the evolution of the filament was mainly due to the geostrophic flows associated with the eddy pair. Our observations reveal the mass exchange of the eddy pair and suggest that submesoscale flows can degrade the coherence of mesoscale eddies, providing important implications for the transport properties of mesoscale eddies. Vigorous submesoscale turbulence was found within the eddy core region, due to filamentous intrusion and frontogenesis. Our findings have thus offered novel insights into the dynamics and transport properties of oceanic submesoscale flows, which should be taken into account in their simulation and parameterization in ocean and climate models.

SIGNIFICANCE STATEMENT: Mesoscale eddies, with a spatial scale from tens to hundreds of kilometers, are ubiquitous in the global ocean. Carrying the largest proportion of oceanic kinetic energy, mesoscale eddies play a key role in ocean dynamics and have important applications for marine biology. Although mesoscale eddies have been studied extensively over the past decades, there are two major issues that remain inconclusive: (i) How do mesoscale eddies dissipate? (ii) Can eddies coherently trap waters when moving over a long distance? Recent studies, mostly through computer simulations, suggest that oceanic submesoscale processes, with a typical scale of a few kilometers, are highly relevant to the above two issues. This study presents a rare observation of a filament intruding into a cyclonic eddy. Because of this filament intrusion, submesoscale activities are enhanced near the eddy core area, in contrast to previous observations that normally suggest weaker submesoscale activities in the eddy core area than at eddy peripheries. Such dedicated process-oriented observations provide unique opportunities for better understanding the dynamics and transport properties of mesoscale eddies and submesoscale processes.

KEYWORDS: Eddies; Mesoscale processes; Transport; Turbulence

1. Introduction

Mesoscale eddies are a prominent feature of the global ocean circulation and play crucial roles in oceanic mass transport, energy transfer, biogeochemical processes, and hence the equilibrium of the ocean general circulation and the global climate system (Chelton et al. 2007, 2011b; Ferrari and Wunsch 2009; Klein and Lapeyre 2009; McGillicuddy et al. 1998; Wunsch and Ferrari 2004). Despite this well-recognized significance, a number of fundamental issues related to mesoscale eddies remain poorly understood, including their energetics, predictability, and interactions with the topography, mean flow, and several other types of oceanic motions like internal gravity waves (Ferrari and Wunsch 2009; Gula et al. 2016; Lee and Niiler 1998; Meng et al. 2021).

Eddy-induced transport and its dynamics are typical outstanding problems among the ones mentioned above. Based on a reduced-gravity model with nonlinear quasigeostrophic dynamics, Early et al. (2011) found that mesoscale eddies, of which the outer edge was defined by zero relative vorticity contour, managed to trap water mass propagating over thousands of kilometers subject to a small amount of water leakage. In line with this work, Zhang et al. (2014) globally estimated the transport caused by mesoscale eddies that are constrained by the outmost closed potential vorticity contours; they found that eddy-induced volume transport is comparable to the large-scale wind-driven circulation. However, an increasing number of studies have shown that the volume transport by mesoscale eddies is substantially overestimated in the Eulerian framework as opposed to the Lagrangian framework (Abernathey and Haller 2018; Cetina-Heredia et al. 2019; Wang et al. 2015).

Supplemental information related to this paper is available at the Journals Online website: https://doi.org/10.1175/JPO-D-22-0189.s1.

Corresponding authors: Hongyang Lin, hylin@xmu.edu.cn; Zhiyu Liu, zyliu@xmu.edu.cn

DOI: 10.1175/JPO-D-22-0189.1

Previous estimates of eddy transports are further challenged by updated understanding of the coherence of mesoscale eddies with the aid of high-resolution numerical simulations and observations. Based on idealized eddy-resolving simulations (1/10°), Liu et al. (2019) suggest that about half of the Eulerian eddies (with lifespan > 30 days) have no coherent cores, which means some half of the water initially within the eddies flows out as they propagate westward. As numerical simulations start to admit or even resolve submesoscale flows, the coherence of mesoscale eddies is seen to be greatly degraded, indicating the importance of submesoscale turbulence in affecting the mass transport of mesoscale eddies (Sinha et al. 2019). Both numerical simulations and observations highlight the role of submesoscale turbulence in regulating the horizontal and/or vertical transport of floating materials or tracers (Balwada et al. 2021; Barkan et al. 2019; D'Asaro et al. 2018). Observations have revealed that interactions of warm-core rings and the shelf break can cause direct onshore intrusion in the form of finer-scale structures and substantial mass leakage from the rings (Zhang and Gawarkiewicz 2015). It is important to note, however, that eddy-resolving observations remain rather challenging to implement, and to date most studies on the coherence of mesoscale eddies and their finer-scale structures are based on numerical simulations.

Oceanic energy cascade related to mesoscale eddies is another important but unresolved issue. The World Ocean is a dynamical system that gains mechanical energy from the atmosphere mainly at the basin scale. This energy is eventually dissipated into heat at the microscale. The dissipation of mesoscale eddies is an important component of the oceanic energy cascade, and is thus crucial to the global ocean energy budget. However, the exact routes and the underlying mechanisms, in particular the dissipation of mesoscale eddies, remain poorly understood (Ferrari and Wunsch 2009). With the increasing capability of high-resolution field observations (in particular through towed systems) and numerical simulations, recent studies have shown that submesoscale flows can provide a conduit for mesoscale eddies to transfer their mechanical energy downscale and eventually be dissipated via small-scale turbulence (Capet et al. 2008; McWilliams 2016; Yang et al. 2017). Both field observations (Yang et al. 2017; Zhong et al. 2017) and numerical simulations (de Marez et al. 2020; Schubert et al. 2020) indicate the existence of active submesoscale flows at the periphery of mesoscale eddies, where submesoscale instabilities (e.g., mixed layer baroclinic instabilities, symmetric instabilities) and strain-induced frontogenesis are prone to develop (Buckingham et al. 2021; Dong et al. 2021, 2022; Fox-Kemper et al. 2008; Hoskins 1982; Taylor and Ferrari 2010; Thomas et al. 2013). However, the spatial and temporal variabilities of submesoscale turbulence within mesoscale eddies and the associated energy transfers remain elusive.

Submesoscale filaments have been increasingly resolved in satellite observations (Choi et al. 2019; Hsu et al. 2020; Li et al. 2017) (particularly visible and infrared images) and in high-resolution numerical simulations (Gula et al. 2014; Sullivan and McWilliams 2017; Zheng and Jing 2022). Their field observations, however, are very difficult to implement, due to their limited cross-frontal scales, their relatively fast evolving nature and the spatial heterogeneity; hence it requires high resolution both in space and time to resolve submesoscale filaments. Observations suggest that dense filaments (Bécognée et al. 2009; Li et al. 2017; Lin et al. 2023; Peng et al. 2020, 2021; von Appen et al. 2018) appear to be more prevalent than light filaments (Shi and Wang 2020; Zhang and Gawarkiewicz 2015), presumably due to the fact that they have a higher rate of sharpening (McWilliams et al. 2009; Sullivan and McWilliams 2017). Additionally, the secondary circulation in the cross-front plane tends to play a role in the frontolysis of light filaments (McWilliams 2016). Observations show that submesoscale dense filament has a convergent velocity field and hence gathers materials at the surface frontal zone (von Appen et al. 2018), as anticipated by pervious numerical studies (McWilliams et al. 2009). Process studies show that atmospheric forcing and the shear of ageostrophic circulation can modulate upper-ocean mixing and stratification of the submesoscale front (Johnson et al. 2020). However, the structures, dynamics and transport properties of filaments remain poorly understood.

In this study, we report on an elaborate observation of a light filament intruding into a cyclonic mesoscale eddy, realized by integrating observations using satellite remote sensing, shipboard field campaign, and the trajectory of a surface drifter. The paper is structured as follows. Section 2 describes the field campaign and methods. Sections 3 and 4 present an overview of the filament structure in both the horizontal and vertical directions, followed by an analysis of the evolution of the filament in section 5. Submesoscale features and momentum balance within the cyclonic eddy are studied in sections 6 and 7. Discussions and summaries are presented in sections 8 and 9.

2. Observations and methods

a. *Field measurements*

From 17 March to 17 April 2019, a cruise targeted at investigating the physical–biogeochemical interactions within mesoscale eddies was implemented with the R/V *Tan Kah Kee* in the North Pacific Ocean subtropical countercurrent (STCC) region. Towed measurements of the upper-ocean temperature, salinity, and biogeochemical variables (e.g., chlorophyll and dissolved oxygen) were conducted using a Moving Vessel Profiler (MVP; AML Oceanographic). The horizontal spacing between two neighboring MVP profiles varies from 3.3 to 6.2 km, depending on the ship speed, with an average of approximately 5 km. The upper-ocean horizontal velocities were recorded continuously throughout the cruise using a shipboard acoustic Doppler current profiler (ADCP). The ADCP velocity data were collected from 9.7 to about 167.7 m with a vertical spacing of 2 m and a horizontal spacing of about 300 m. In addition, an underway thermosalinograph SBE21 (Sea-Bird Scientific) was used to measure near-surface (~5 m) temperature and salinity throughout the cruise. The sampling time interval of the thermosalinograph SBE21 was 10 s (corresponding to a horizontal spacing of about 50 m).

b. *Eddy identification and tracking*

We implement eddy detection and tracking following the algorithms of Mason et al. (2014). Eddy boundary is defined

as the contour of maximum azimuthally averaged geostrophic velocity. Here we define the eddy center as the position of extreme values of the sea level anomaly (SLA) within the eddy.

c. Calculation of the relative vorticity and stain rate

Assuming that the role of curvature is negligible and that the velocity has no variations in the cross-sectional direction y, the formulations of the relative vorticity and stain rate reduce to

$$\xi = \partial v/\partial x \quad \text{and} \tag{1}$$

$$\text{strain} = \sqrt{\left(\frac{\partial u}{\partial x}\right)^2 + \left(\frac{\partial v}{\partial x}\right)^2}, \tag{2}$$

where u and v are the zonal and meridional velocity components and x and y are the zonal and meridional directions, respectively.

d. Lagrangian particle tracking experiment

The Lagrangian particle tracking simulations are conducted using the OceanParcels package (Delandmeter and van Sebille 2019; Lange and van Sebille 2017), which is based on a fourth-order Runge–Kutta scheme to simulate particle trajectories. Virtual passive particles are released inside selected regions, and then are allowed to freely evolve under the advection of the altimeter-derived geostrophic currents. Diffusions (i.e., advections due to unresolved flows) are not considered.

e. Calculation of the frontogenesis function

The frontogenesis function F is calculated using surface geostrophic currents from gridded altimeter data and sea surface density derived from *Himawari-8* SST data (assuming a constant salinity value of 35 g kg^{-1}) (Hoskins 1982; Mahadevan 2016):

$$F = -\left(\frac{\partial u}{\partial x}\frac{\partial \rho}{\partial x} + \frac{\partial v}{\partial x}\frac{\partial \rho}{\partial y}\right)\frac{\partial \rho}{\partial x} - \left(\frac{\partial u}{\partial y}\frac{\partial \rho}{\partial x} + \frac{\partial v}{\partial y}\frac{\partial \rho}{\partial y}\right)\frac{\partial \rho}{\partial y}, \tag{5}$$

where ρ is potential density. The velocity data are interpolated onto the same grids as the density field in the calculation.

f. The thermal wind balance

Both density data and velocity data are horizontally low-pass filtered with a cutoff wavelength of ~10 km. Then the velocity data are interpolated onto the same grids as the density field. In this study we compare the vertical shear of meridional velocities and the horizontal buoyancy gradient in the zonal direction to check the validity of the thermal wind balance:

$$\frac{\partial v}{\partial z} = -\frac{g}{f\rho_0}\frac{\partial \rho}{\partial x}, \tag{6}$$

where g is the acceleration due to gravity, f is the Coriolis parameter, and ρ_0 is a reference density (1022 kg m^{-3}).

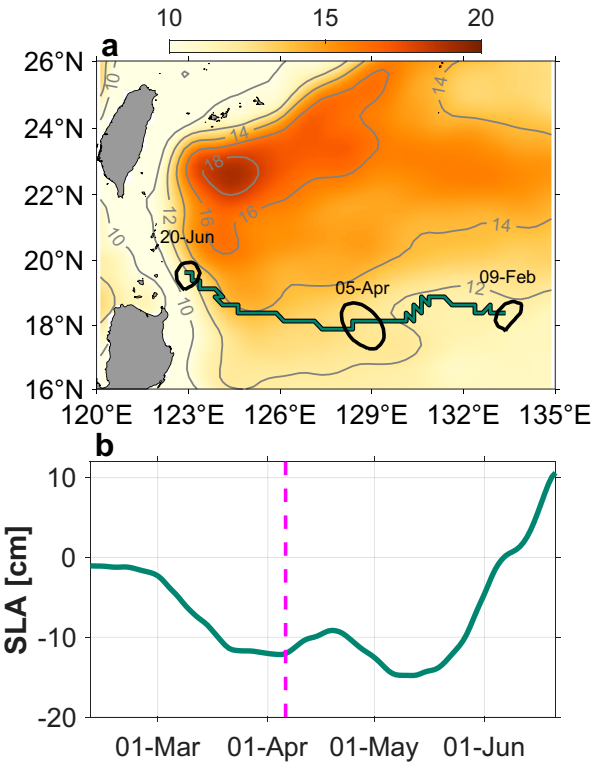

FIG. 1. Eddy activities in the study region and the evolution of the observed eddy: (a) Root-mean-square sea level anomaly (SLA) (cm) in the northwestern Pacific Ocean based on gridded altimeter data from January 1993 to December 2019. Black thick circles indicate the edge of the observed cyclonic eddy (CE) at the dates when it was generated (east), observed (middle), and degenerated (west). The green curve indicates the eddy trajectory. (b) Time series of SLA (cm) in the center of CE. The magenta dashed line indicates 5 Apr when the filamentous intrusion was observed (shown in Fig. 2).

3. Filamentous intrusion

The STCC region is one of the most energetic areas in terms of mesoscale eddy activities in the North Pacific Ocean (Qiu 1999). A series of mesoscale eddies (mostly cyclones) were sampled during the field campaign. In this study, we focus on the observation of a cyclonic eddy with the most intense field measurements (hereinafter CE). Based on the result of eddy identification and tracking procedures, CE first appeared at 18.3°N, 133.5°E on 9 February 2019 and disappeared at 19.5°N, 123°E on 20 June 2019 after interacting with the Kuroshio (Fig. 1a). Field measurements of CE were conducted from 19 March to 14 April (in two separate stages, with stage 1 from 19 to 20 March and stage 2 from 28 March to 14 April). The time series of SLA in the center of CE shows that it intensified (10 February–20 March), matured (20 March–18 May), and decayed (19 May–20 June) (Fig. 1b). There is an anticyclonic eddy (hereinafter AE) immediately to the west of CE (Figs. 2a,b; see also Fig. S3 in the online supplemental material with a different color map), thus forming an eddy pair, which moved westward for months. Enhanced meridional

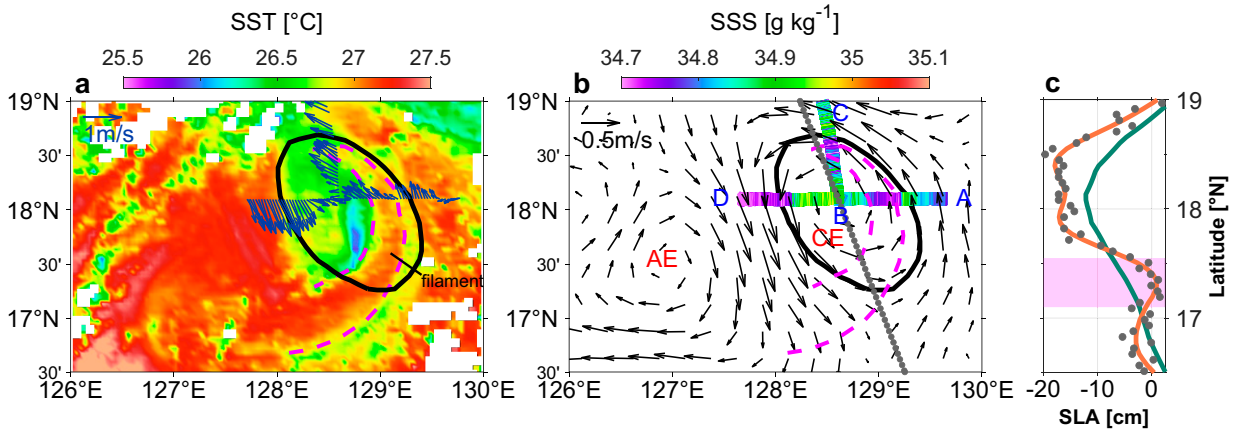

FIG. 2. Sea surface temperature, salinity, currents, and SLA: (a) SST (°C) from MODIS *Terra* infrared imager on 5 Apr. Also shown are shipboard-ADCP-measured near-surface (~10 m) velocities (arrows) along the ship track. The magenta dashed lines indicate the filament outline (visual identification combining SST and its gradient). (b) Geostrophic velocities estimated from the gridded altimeter data (arrows) and the near-surface (~5 m) salinity (g kg^{-1}) from the underway SBE21 (colored). The magenta dashed lines indicate the filament outline as in (a). The ship path follows A → B → C → B → D. The black thick curves in (a) and (b) indicate the edge of CE. The gray dots indicate the (along track) sampling points of the altimeter. (c) SLA (cm) from along-track and gridded altimeter data. Gray dots indicate raw, along-track SLA, and the orange curve shows their low-pass filtered version (by removing instrumental white noises associated with surface waves); the green curve indicates the gridded SLA but interpolated onto along-track altimeter sampling points. The magenta shading indicates the position of the filament.

velocities were found at the edge of CE. Strikingly, there was a strong jet with a velocity exceeding 0.8 m s^{-1} saddled between the eddy pair, and relatively large gradients in both temperature and salinity were present associated with this jet (Figs. 2a,b).

During the cruise, a warm filament was observed to intrude into CE from Moderate-Resolution Imaging Spectroradiometer (MODIS) sea surface temperature (SST) data on 5 April (Fig. 2a). The outline of the warm filament is depicted using the MODIS SST image (bounded by magenta dashed lines in Fig. 2a), and it is evident that the filament outline exactly matches the low-salinity portions of the two transects (AB and BC) with ship-based underway measurements (Fig. 2b). This suggests that the intruded filament is relatively warm and fresh, and hence of low density, in comparison with the ambient water. We thus call it a light filament. The near-surface velocities from the shipboard ADCP show an intensified northward flow at the western periphery of the filament but a weakened northward flow at the eastern end (Fig. 2a). This flow pattern associated with the filament seems to be in line with the thermal wind balance, and the horizontal velocity shear suggests it to be an anticyclonic-like filament. Moreover, SLA from the along-track altimetry shows evident elevated sea level within the filament (the bump within the magenta shading in Fig. 2c; ~17.1°–17.6°N), consistent with its anticyclonic-like nature. By contrast, SLA from gridded altimeter data shows almost no abnormal signal within the filament, indicating the incapability of resolving submesoscale flows by the gridded product. Besides, the along-track SLA also shows larger gradients than the gridded data. To conclude, the manifestations associated with the filament discussed above (i.e., relatively high temperature, low salinity, high SLA, and flow pattern) all indicate the consistency between the remote sensing observations and near-surface field measurements. In short, we observed a warm and fresh (and thus light) anticyclonic-like filament intruding into a cyclonic eddy.

4. Vertical structure

We now examine the vertical structure of the eddy pair based on towed thermohaline measurements with the MVP and underway velocity measurements with the shipboard ADCP along a zonal section across CE and part of AE (section AB–BD in Fig. 2b). The observed part of AE was relatively warm and fresh, whereas the upwelled subsurface cool and salty water occupied the core area of CE resulting in mesoscale domed isopycnals interleaved with smaller-scale vertical excursions (Figs. 3a–c; see also Fig. S4 in the online supplemental material with a different color map). In particular, a finer-scale (submesoscale) pycnocline bump was observed in the eddy center (~128.75°E); it corresponded well with the cold patch just west of the filament (Fig. 2a). If the density data are horizontally low-pass filtered with a cutoff wavelength of 150 km (on scales above which the sea surface height can be readily resolved by gridded altimeter data; Chelton et al. 2011a; Ducet et al. 2000), the smoothed isopycnals correspond well with the negative gridded SLA of CE in terms of the location of the eddy center (Fig. 3d). This suggests that the gridded altimeter data well captured the mesoscale structure of CE. The vertically out-of-phase correspondence of SLA and isopycnals, as well as the magnitude of their vertical elevation, is a clear manifestation of the first baroclinic mode nature of typical oceanic surface-intensified eddies. The sectional

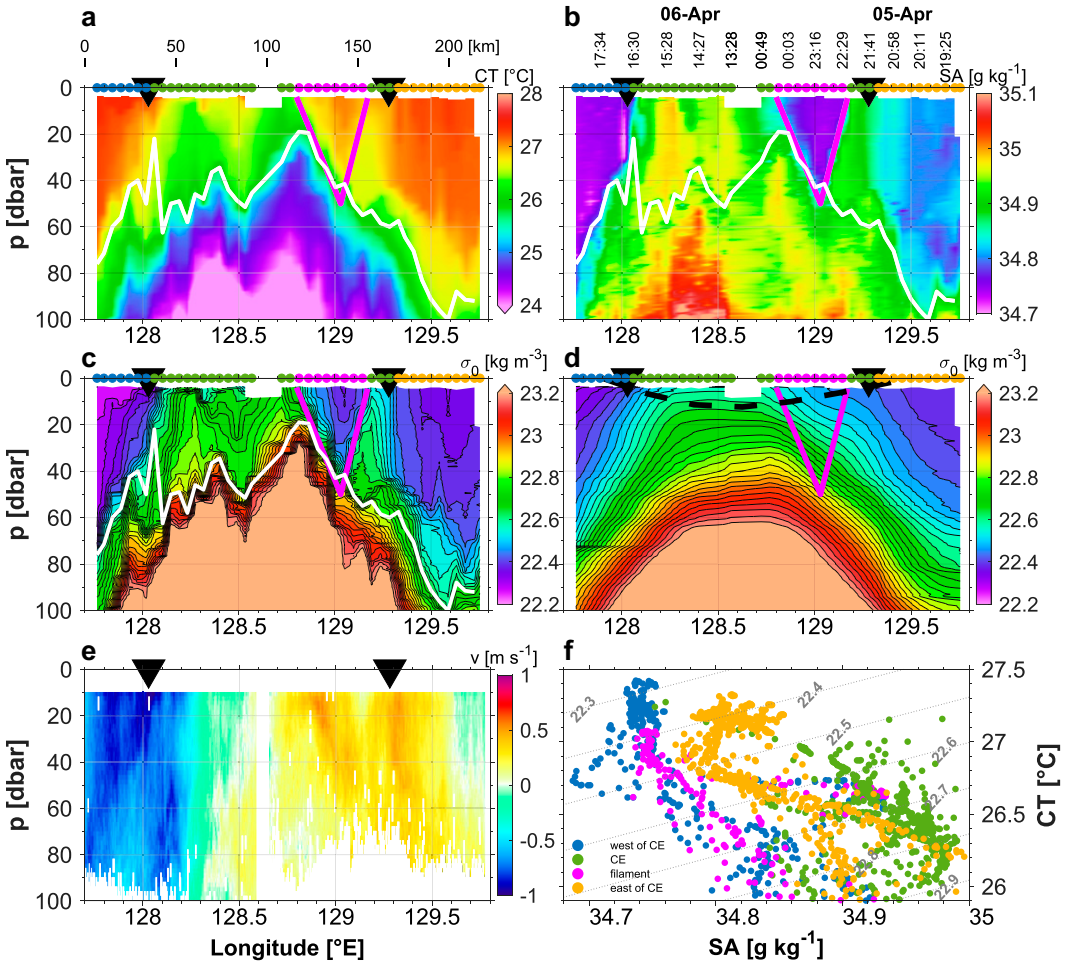

FIG. 3. Sectional distribution of measured variables along the zonal transect AB–BD: (a) conservative temperature (°C), (b) absolute salinity (g kg^{-1}), (c) potential density anomaly (kg m^{-3}; black contours indicate isopycnals from 22.2 to 23.21 kg m^{-3}, with an interval of 0.03 kg m^{-3}), (d) low-pass-filtered potential density anomaly (kg m^{-3}) with a cutoff horizontal wavelength of 150 km [the black dashed line indicates SLA but magnified by a factor of −100, and black contours are the same as in (c)], and (e) meridional velocity (m s^{-1}). (f) A *T*–*S* diagram; the color of the dots indicates data from the different positions as given in (a)–(d). In (a)–(e), black triangles indicate the eddy edges; colored dots on the top axis indicate the positions: west of CE (blue), within CE (green), within the filament (magenta), and east of CE (yellow); magenta lines indicate the outline of the filament; and white lines indicate the depth of the mixed layer base (0.3 kg m^{-3} greater than the density at 10-m depth). The distance coordinate and actual time (UTC) of the observation are added above the top axis of (a) and (b), respectively.

distribution of meridional velocity shows intensified flows at the eddy peripheries (Fig. 3e), accompanied by maximum tilts of isopycnals and strong fronts (Fig. 3c), in accord with the thermal wind balance.

In the eastern part of CE, the filament is characterized by a wedge of water within the mixed layer featured with high temperature, low salinity, and hence low density (bounded by magenta lines in Figs. 3a–c). The depressed isopycnals of the filament (Fig. 3c) also correspond well with its locally elevated SLA (along-track altimetry observations shown in Fig. 2c) in the context of the first baroclinic mode. The thermal wind balance suggests positive vertical shear of meridional velocity on the western flank of the filament and negative shear on the eastern flank, and given the background northward flow on the eastern side of CE, we expect intensified (weakened) northward flow at the western (eastern) edge of the filament, which is confirmed by the sectional velocity measurements (Fig. 3e). Assuming that the filament transect is a triangle and given the mean northward velocity of the filament transect $v \approx 0.36$ m s^{-1}, the width of the filament near the surface $W \approx 42$ km, and the depth of the filament $H \approx 50$ m, we can estimate a northward volume transport of the warm and freshwater $Q_v \approx 0.38$ Sv (1 Sv $\equiv 10^6$ m^3 s^{-1}).

Further inspection of Figs. 3a and 3b and the *T*–*S* diagram (Fig. 3f) suggests that the filament has almost the same thermohaline characteristics (i.e., warm and fresh) with AE (west of the jet). Recalling the plane shape of the filament, this

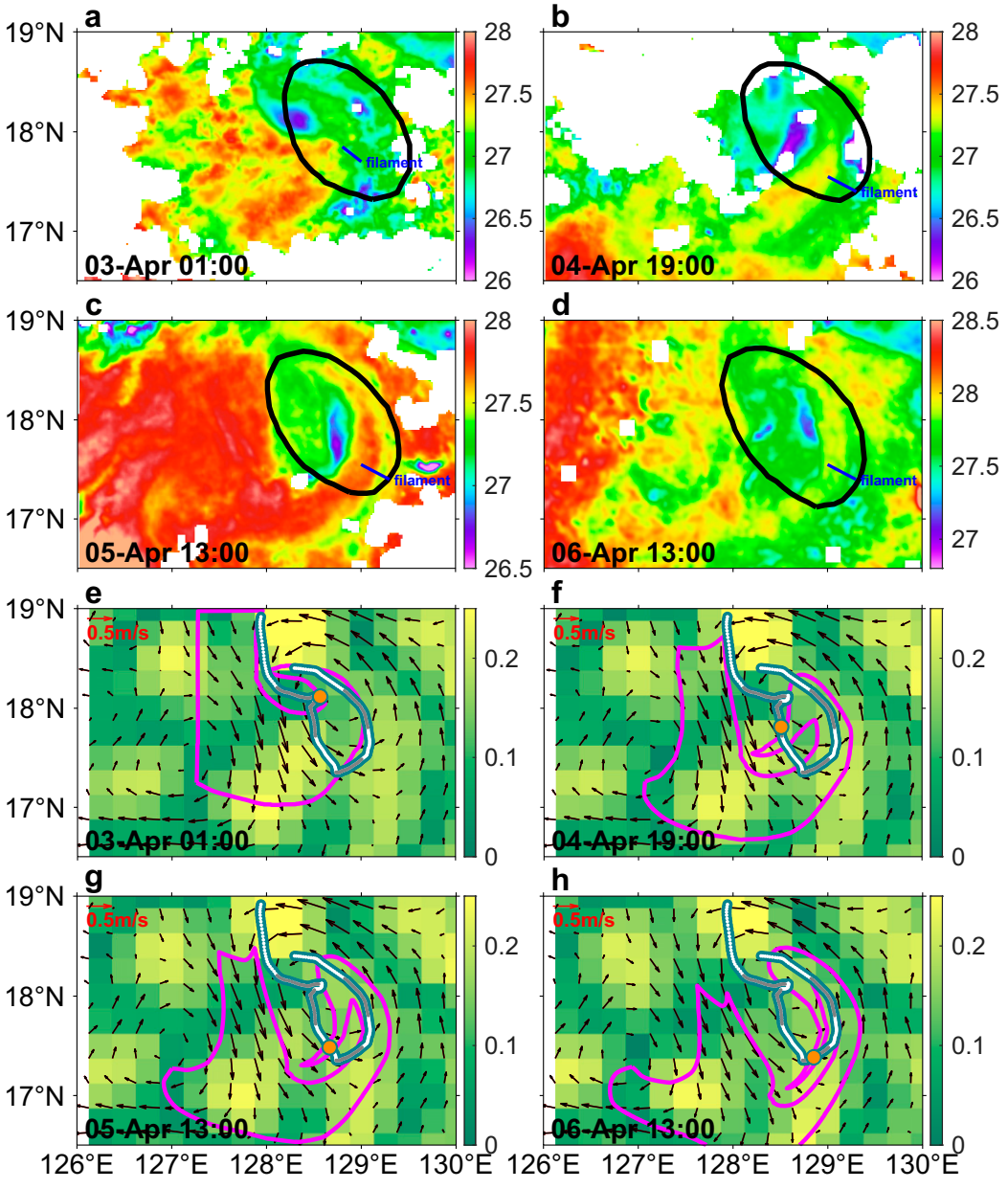

FIG. 4. (a)–(d) SST (°C) from *Himawari-8* (colors) and (e)–(h) strain rate calculated from surface geostrophic velocity (colors) on 3–6 Apr 2019 [5-h mean SST data are used in (a), and hourly mean data are used in (b)–(d)]. The black thick curves in (a)–(d) indicate the eddy edge. The strain rate is normalized by the local planetary vorticity *f*. Also shown in (e)–(h) are geostrophic velocity (arrows) and the outline of passive particles (magenta curves). The white and gray curve in (e)–(h) indicates the pathway of a drifter (WMO: 2201552) on 1–9 Apr 2019 with white and gray denoting odd and even days, respectively. The orange dot in (e)–(h) marks the same time with SST images in (a)–(d).

thermohaline similarity inspires us to conjecture that the filament might originate from the neighboring AE.

5. Evolution of the filament

To backtrack the origin of the light filament, high-resolution SST images from *Himawari-8* are used to examine the filament's evolution (Fig. 4). On 3 April, a portion of warm water intruded into CE directly from the west (Fig. 4a). Under the southward advection due to the strong jet, the filament continued to intrude into CE, which was migrating southward. On 4 April, the main part of the filament became narrower moving southeastward, and its tip was already entrained into the CE core, rotating along with the mesoscale velocity field (Fig. 4b). In the following two days, the tip of the filament intruded farther into CE's interior (Figs. 4c,d). The pattern of the filament

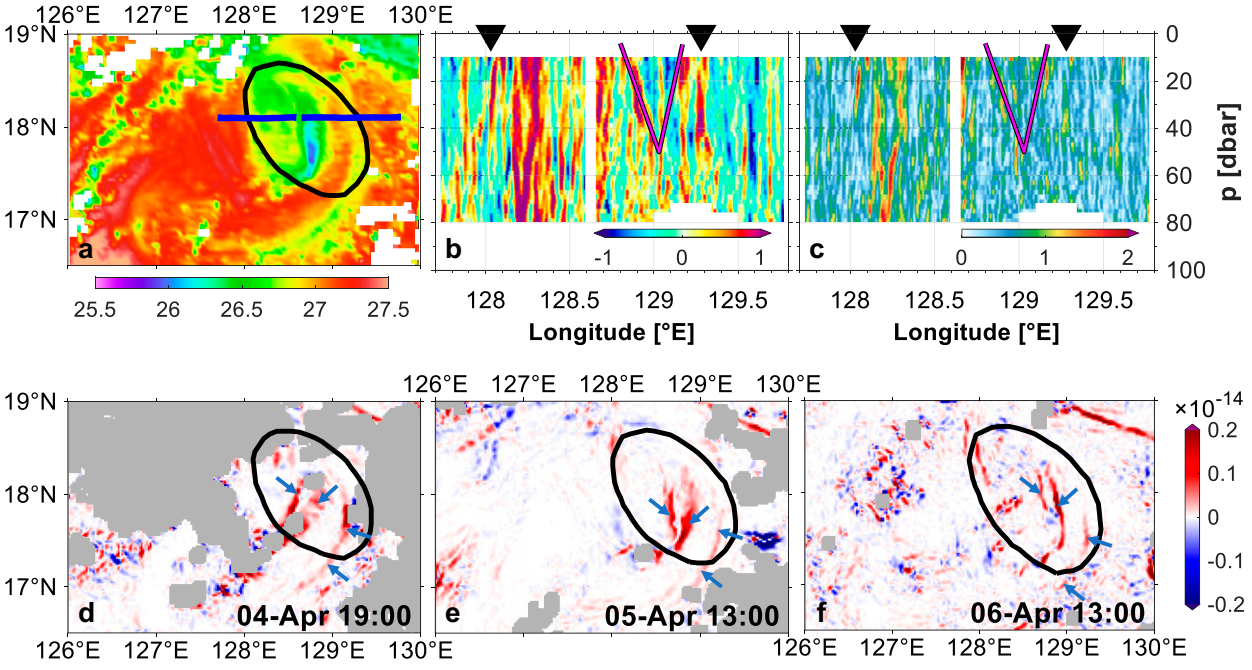

FIG. 5. (a) SST (°C) from MODIS *Terra* infrared imager on 5 Apr. Blue lines indicate the sections shown in (b) and (c). Vertical structure of (b) relative vorticity and (c) strain rate (both normalized by the local planetary vorticity f). Black triangles indicate the eddy edge. Magenta lines indicate the outline of the filament. The blank region near ~128.65°N is due to the discontinuity of the data. (d)–(f) The frontogenesis function ($kg^2\ m^{-8}\ s^{-1}$) on 4–6 Apr 2019, respectively. The black thick curves indicate the eddy edge. The blue arrows indicate frontogenesis regions. Regions with missing data are shaded in gray.

in SST image on 5 April was very similar to that from MODIS (Fig. 2a). On 6 April, the western part of the filament (its base) started to lose its coherent structure. These satellite observations seem to support our hypothesis that the filament originated from the neighboring anticyclonic eddy.

To further investigate the role of the background mesoscale currents in the filament evolution, we conducted a Lagrangian particle tracking experiment based on the altimeter-derived geostrophic velocities. Virtual passive particles were released inside the filament region (inside the magenta curve in Fig. 4e, whose east and south boundaries are defined by SST fronts) on 3 April, and then were allowed to freely evolve under the advection of geostrophic currents (Figs. 4e–h). The evolution of the released particles was similar to the evolution of the filament from SST images, except for some differences in the tip. One can also see slightly enhanced mesoscale strain in the filament region. This partially confirms that the evolution of the filament was dominated by the mesoscale velocity field and the filament should be a coherent structure.

Coincidently and luckily, there was also a drifter that moved from outside the eddy pair into CE during the cruise (Figs. 4e–h and Fig. S1 in the online supplemental material). The drifter's trajectory (white and gray curves) also reveals the filament's evolution. The drifter first moved along the northern part of the jet on 1 April, and then somewhat unexpectedly moved across the western boundary of CE toward the eddy center and along the northern boundary of the filament on 2 April. In the next few days (3–6 April), the drifter generally moved together with the filament under the background mesoscale velocity field. Except for 2 April, the trajectory of the drifter was largely consistent with the filament evolution due to mesoscale advection, as depicted above. The trajectory of the drifter on 2 April was almost orthogonal to the geostrophic velocity vectors (the trajectory also traversed the material transport lines defined by the finite-time Lyapunov exponents; Fig. S2 in the online supplemental material), indicating existence of finer-scale (submesoscale) flows that were unresolved by the gridded altimeter data. Indeed, such a trajectory is in line with our expectation of an intensified eastward flow at the northern periphery of the filament according to the thermal wind balance.

Combining satellite SST images, particle-tracking simulation, and the trajectory of the drifter, we infer that the evolution of the filament on 3–6 April was largely controlled by the advection of mesoscale geostrophic flows. Combining the plane shape of the filament, thermohaline similarity between the filament and AE, and coherence of the filament, we conclude that the warm and fresh filament originated from the neighboring AE. There are also indications of the existence of submesoscale flows within CE that could not be resolved by the gridded altimeter data. Moreover, our observations provide direct evidence of water exchange between the eddy pair, indicating the role of submesoscale turbulence in impacting the coherence of a mesoscale eddy.

6. Vigorous submesoscale turbulence within CE

To study submesoscale features within CE, we calculate the relative vorticity ζ and strain rate, along section AB–BD

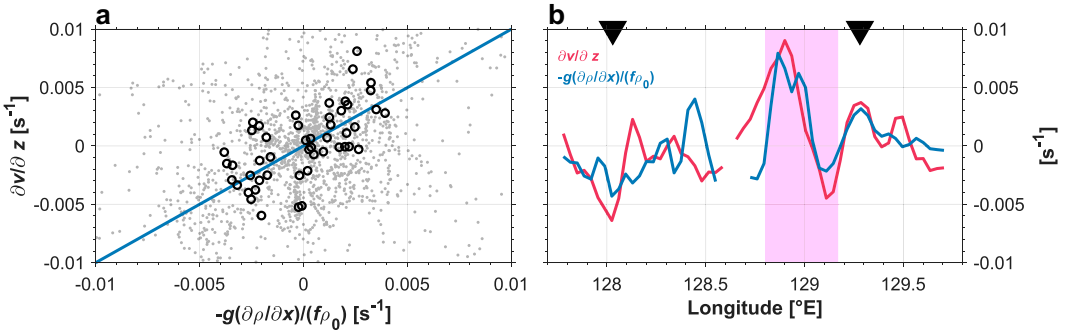

FIG. 6. Verification of the thermal wind balance: (a) Comparison between vertical shear of meridional velocities and horizontal buoyancy gradient for the AB–BD section within the upper 80 m. Original data are shown as gray dots, and the box-averaged (26 km in the along-transect direction and 10 m in the vertical direction) samples are the black open circles. The blue line indicates the one-to-one relation. (b) Vertically averaged velocity shear (red lines) and horizontal buoyancy gradient (blue lines) within the upper 50 m. Magenta shading indicates the position of the filament. Black triangles indicate the eddy edge. The break near ~128.65°N is due to the discontinuity of the data.

(Figs. 2b and 5a) using ADCP data (Figs. 5b,c). There was large $\zeta/f \sim O(1)$ at the peripheries of CE, consistent with previous studies (Yang et al. 2017). Interestingly, there was also large $\zeta/f \sim O(1)$ in the eddy core region. Specifically, relatively large positive ζ/f was observed at the edges of the filament while large negative ζ/f was present inside the filament, indicating active submesoscale flows within the filament. Large ζ/f and strong strain rate were also observed near the eddy center where the abovementioned cold patch was located (Figs. 3a and 5a). Without direct influence of the filament, the western part of CE (128.1°–128.2°E) was also characterized by large ζ/f and strong strain rate (Figs. 5b,c).

The diagnosed frontogenesis function [Eq. (5)] using satellite-derived geostrophic velocity and SST data also shows elevated values at the peripheries of the cold patch and the filament (Figs. 5d–f). This suggests that the observed energetic submesoscale flows within CE might be due to frontogenesis. The SST images also revealed that the structure of the warm filament got increasingly fine during its intrusion (Figs. 4a–d), which might be a manifestation of frontogenesis. Elevated frontogenesis function values were also found at the northwestern corner of CE, where a strong temperature front and jet existed (Figs. 4c,d and 5e,f).

Note that the frontogenesis function calculated here should be mesoscale-induced frontogenesis as the surface geostrophic velocities obtained from gridded altimeter data can only resolve mesoscale currents (large-scale currents are also included but can be negligible here). The reliability on the calculation of frontogenesis function is examined in section 8.

7. Momentum balance of CE and the filament

Our precedent analysis indicates that both CE and the filament qualitatively satisfy the thermal wind balance. There were also relatively vigorous submesoscale flows associated with the filament that seem to deviate from the balanced dynamics. To check to what extent the filament can be taken as a balanced feature, we compare the vertical shear of meridional velocities and the horizontal buoyancy gradient for the zonal section across CE (AB–BD, Fig. 2b). These two terms are calculated using ADCP and MVP data for the upper 80 m (below which the quality of ADCP data was poor). We also calculate box averaged values of the two terms. The size of the box is chosen to be 26 km in the along-transect direction and 10 m in the vertical direction. It is evident from Fig. 6a that the box-averaged values approximately follow the diagonal that represents exact thermal wind balance. This means along the entire section across CE the flow largely obeyed the thermal wind balance. The scattering of the original data (gray dots) implies that the box average may have filtered out velocities that are not in geostrophic balance or errors in currents/thermohaline observations. We now vertically average (upper 50 m; i.e., the depth range of the filament) the two terms to examine the longitudinal dependence of the validity of the balance. It is clear that the two terms matched each other well within the filament (magenta shading in Fig. 6b) and the eastern edge of CE. Interestingly, the agreement between the two terms was comparably degraded for the western part of CE where the influence of the filament was limited and the magnitudes of the terms were both relatively small. Overall, these results suggest that both CE and the filament can be taken as balanced features.

Previous studies based on realistic high-resolution numerical simulations indicate that the turbulent thermal wind balance, instead of the standard thermal wind balance, is more suitable to describe the dynamics of elongated filaments (Gula et al. 2014). Probably due to its relatively large size, the light filament observed in this study seems to be well described by the standard thermal balance.

8. Discussion on the calculation of frontogenesis function

The gridded altimetry data can only resolve flows with a horizontal scale > 150 km (Chelton et al. 2011a; Ducet et al. 2000), whereas the high-resolution (~2 km) SST images from *Himawari-8* can partly resolve submesoscale features. Here we

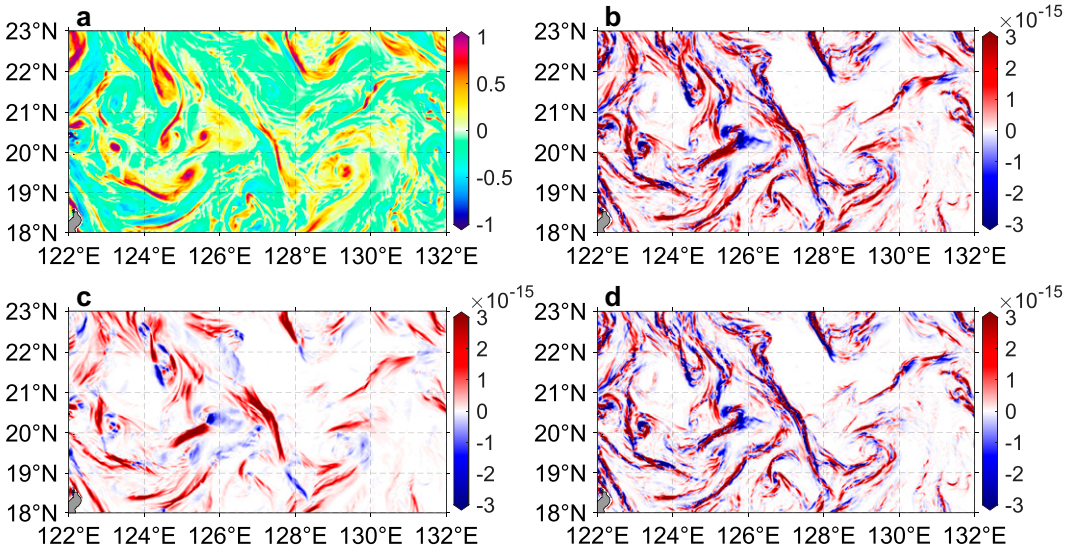

FIG. 7. (a) Rossby number, and the frontogenesis functions ($kg^2\ m^{-8}\ s^{-1}$) calculated from MITgcm LLC4320 output based on (b) raw currents, (c) mesoscale currents, and (d) submesoscale currents.

check whether frontogenesis function calculated from mesoscale currents and high-resolution SST can actually characterize oceanic frontogenesis. Specifically, we use high-resolution (~2 km) numerical simulations in the STCC region from MITgcm LLC4320 to investigate the contribution of mesoscale currents to frontogenesis. This model output has been widely used to study regional or global submesoscale features, and detailed configurations as well as various validations of the simulation can be found in the literature (e.g., Lin et al. 2020; Qiu et al. 2018; Wang et al. 2022). We first apply a 3-day (4–6 April 2012) average on surface data (currents, temperature, and salinity) to remove the tidal signal and then decompose the currents into mesoscale and submesoscale currents (simply via horizontal low-pass and high-pass filtering with a cutoff wavelength of 150 km):

$$\mathbf{u} = \mathbf{u}_{\text{meso},>150\text{km}} + \mathbf{u}_{\text{submeso},<150\text{km}}. \tag{7}$$

Note that the simple technique used here is not expected to work well in decomposing mesoscale and submesoscale motions, but just to verify the reliability of using frontogenesis function to indicate the active level of submesoscale flows within CE. The reason to choose a relatively large cutoff wavelength is that altimeter-derived geostrophic currents only resolve signals with a scale of >150 km (Ducet et al. 2000). Large-scale currents are also included in the decomposed "mesoscale" band but their effect on frontogenesis is negligible in the STCC region. We then calculate the frontogenesis function using the raw, mesoscale, and submesoscale currents, respectively (Fig. 7).

Energetic submesoscale motions with high Rossby number Ro can be recognized in the STCC region (Fig. 7a). The high-Ro areas are also collocated with large values of the frontogenesis function F (Fig. 7b). The mesoscale-induced frontogenesis function F_{meso} can capture the general pattern of F, although many finer-scale structures are missing (Figs. 7b,c). By contrast, the submesoscale-induced frontogenesis function F_{submeso} highly resembles the distribution of F (Figs. 7b,d).

The scatterplot indicates a relatively good linear relationship between F_{meso} and F (Fig. 8a), suggesting the usefulness of F_{meso} in representing the general features of F. The scatterplot exhibits a much closer linear relationship between F_{submeso} and F (Fig. 8b), as expected from their spatial distributions (Figs. 7b,d). The slopes from linear regressions (i.e., 0.128 and 0.872) indicate the respective contributions of mesoscale (12.8%) and submesoscale (87.2%) currents to F because the intercept ($\pm 0.065 \times 10^{-14}\ kg^2\ m^{-8}\ s^{-1}$) is negligible. The probability density functions (PDF) of F_{meso}/F and F_{submeso}/F both show a domination of positive values (Figs. 8c,d; 79% and 97%, respectively). Therefore, when measurements at the submesoscale resolution are not available, F_{meso} can qualitatively represent the pattern of frontogenesis using mesoscale currents and high-resolution sea surface temperature or density measurements. Our previous estimates of the frontogenesis function within CE bear some reliability.

The fact that the general patterns of F_{meso} and F_{submeso} resemble each other (Figs. 7c,d) might be due to two reasons. First, the submesoscales are generated by the mesoscale strain-induced frontogenesis. Second, it is also possible that mesoscale and submesoscale currents have not been well decomposed subject to the simple temporal filter being used. Besides, mesoscale and submesoscale currents are expected to exert a different effect on frontogenesis in time scale, which, nonetheless, is ignored in our statistical analysis. More definitive roles of mesoscale and submesoscale currents on frontogenesis are worthy of further investigation on the basis of more robust, dynamical decomposition methods (e.g., Liang 2016; Wang et al. 2023).

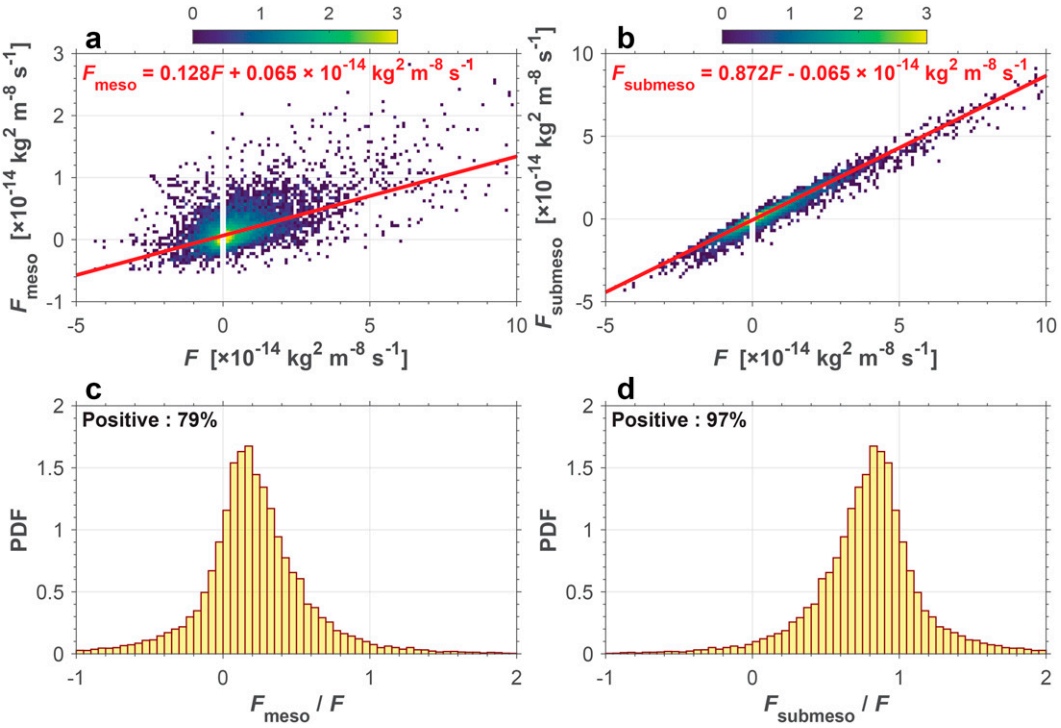

FIG. 8. Scatterplots of (a) F and F_{meso} and (b) F and $F_{submeso}$. The number of points has been taken as the logarithm (colors). Also shown are the probability density functions (PDF) of (c) F_{meso}/F and (d) $F_{submeso}/F$.

9. Summary

In this study, we report on an elaborate observation of a light filament intruding into a cyclonic mesoscale eddy, realized by integrating observations using remote sensing, shipboard field campaign, and the trajectory of a surface drifter. It is demonstrated that the filament was largely a balanced feature accompanied by energetic submesoscale flows. The observed filament had a wedge-shaped structure encompassing a block of warm and freshwater within the mixed layer. This filamentous intrusion caused a 0.38 Sv northward volume transport in the observed transect. This horizontal transport may be mainly induced by the background eddy advection effect, but quantifying the transport of intruded freshwater of an external origin still has important implications on the coherence of mesoscale eddies and eddy-induced transports. Our observations provide direct evidence that the filament intrusion can destroy the mesoscale coherence and cause significant water exchange between the mesoscale eddy and neighboring flow features.

The horizontal velocity shear and the depressed isopycnals suggest that the filament was anticyclonic-like. This corresponds well to the regionally elevated sea surface height based on along-track altimeter data, which, however, was not resolved in the gridded altimeter data. The effectiveness of along-track altimeter data in resolving filament shown here sheds light on the application of the wide-swath altimeter [e.g., Surface Water and Ocean Topography (SWOT)] in improving our knowledge of submesoscale flows in future (Fu and Ubelmann 2014). It is almost certain that submesoscale motions, which are unresolved in the current gridded altimeter data, significantly affect the estimate of surface kinetic energy no matter in cases such as the observed example shown in the present study or in the global context. Our understanding on the coherence of mesoscale eddies, eddy-induced volume transport and submesoscale spatiotemporal variability is expected to be greatly improved after the advent of SWOT.

Combining satellite SST images, particle-tracking simulation, and the trajectory of a surface drifter, we find that the evolution of the filament was largely controlled by the advection of mesoscale geostrophic flows, and the filament likely stemmed from the neighboring anticyclonic eddy. This suggests that mesoscale horizontal advection can play an important role in the formation of oceanic filamentous structures and the deformation of submesoscale flow features.

Because of frontogenesis induced by the intruded filament, energetic submesoscale flows were observed within the eddy core region, in contrast to most previous findings based on field observations or numerical simulations, which normally show active submesoscale flows at the peripheries of mesoscale eddies (Callies and Ferrari 2013; de Marez et al. 2020; Yang et al. 2017). The observations reported in the present study thus add our understanding of the spatial variability of submesoscale turbulence within mesoscale eddies. Our study indicates that vigorous frontogenesis can also happen near the eddy center as the filamentous intrusion results in prominent submesoscale fronts (e.g., the cold patch structure and the filament itself). Our observations highlight the importance of high-resolution observations in advancing

our understanding of the regional dynamics in the context of mesoscale eddies.

It is intriguing to find that frontogenesis function calculated from mesoscale geostrophic currents and high-resolution SST can represent the general features of the realistic oceanic frontogenesis. With the lack of high-resolution surface currents, this finding gives us confidence to infer regional or global frontogenesis processes with available data. With submesoscale currents available from the coming wide-swath satellite missions, oceanic frontogenesis processes are expected to be even refined.

Lacking measurements, we are not able to resolve the generation process of the filament. Further studies using process-oriented measurements and numerical simulations are required to uncover the mechanisms and dynamics related to the generation and dissipation of the filament.

Acknowledgments. This work was supported by the National Natural Science Foundation of China (41730533, 91858201, 42076013, 41890801, and 41721005), and the Natural Science Foundation of Fujian Province of China (2021J02005). We thank Jiang Long and the crew of the R/V *Tan Kah Kee* for their assistance in data collection. Chuanyin Wang, Tianyu Zhou, and Ruixi Zheng are thanked for helpful discussions. We also thank other members of the Dynamical Oceanography Group (DyOG) for their recommendations that have improved this work. We thank Yunpeng Cui for helping download the LLC4320 data. Robin Robertson kindly helped polish the presentation of this paper. We thank the two anonymous reviewers for their constructive suggestions and comments, which have not only helped improve early versions of the paper but also inspired our further work.

Data availability statement. The daily SST data of MODIS at ~4-km resolution are downloaded from the NASA Ocean Data Processing System (https://oceandata.sci.gsfc.nasa.gov/), and the hourly SST data of *Himawari-8* at ~2-km resolution are downloaded from the Japan Aerospace Exploration Agency (https://www.eorc.jaxa.jp/ptree/index.html). The satellite altimeter data are obtained from the Copernicus Marine Environment Monitoring Service (http://marine.copernicus.eu/), including the daily gridded sea level anomaly (SLA), absolute dynamic topography (ADT), and their respective geostrophic velocities at 1/4° resolution, as well as the along-track SLA data of *Jason-3* at ~6.2-km resolution. The drifter data from the Global Drifter Program (GDP) are downloaded from the National Oceanic and Atmospheric Administration (NOAA) Atlantic Oceanographic and Meteorological Laboratory (https://www.aoml.noaa.gov/phod/gdp/data.php). The observational data that were used are available online (https://doi.org/10.17605/OSF.IO/FX8D7).

REFERENCES

Abernathey, R., and G. Haller, 2018: Transport by Lagrangian vortices in the eastern Pacific. *J. Phys. Oceanogr.*, **48**, 667–685, https://doi.org/10.1175/JPO-D-17-0102.1.

Balwada, D., Q. Xiao, S. Smith, R. Abernathey, and A. R. Gray, 2021: Vertical fluxes conditioned on vorticity and strain reveal submesoscale ventilation. *J. Phys. Oceanogr.*, **51**, 2883–2901, https://doi.org/10.1175/JPO-D-21-0016.1.

Barkan, R., M. J. Molemaker, K. Srinivasan, J. C. McWilliams, and E. A. D'Asaro, 2019: The role of horizontal divergence in submesoscale frontogenesis. *J. Phys. Oceanogr.*, **49**, 1593–1618, https://doi.org/10.1175/JPO-D-18-0162.1.

Bécognée, P., M. Moyano, C. Almeida, J. M. Rodríguez, E. Fraile-Nuez, A. Hernández-Guerra, and S. Hernández-León, 2009: Mesoscale distribution of clupeoid larvae in an upwelling filament trapped by a quasi-permanent cyclonic eddy off northwest Africa. *Deep-Sea Res. I*, **56**, 330–343, https://doi.org/10.1016/j.dsr.2008.10.008.

Buckingham, C. E., J. Gula, and X. Carton, 2021: The role of curvature in modifying frontal instabilities. Part I: Review of theory and presentation of a nondimensional instability criterion. *J. Phys. Oceanogr.*, **51**, 299–315, https://doi.org/10.1175/JPO-D-19-0265.1.

Callies, J., and R. Ferrari, 2013: Interpreting energy and tracer spectra of upper-ocean turbulence in the submesoscale range (1–200 km). *J. Phys. Oceanogr.*, **43**, 2456–2474, https://doi.org/10.1175/JPO-D-13-063.1.

Capet, X., J. C. McWilliams, M. J. Molemaker, and A. F. Shchepetkin, 2008: Mesoscale to submesoscale transition in the California Current system. Part I: Flow structure, eddy flux, and observational tests. *J. Phys. Oceanogr.*, **38**, 29–43, https://doi.org/10.1175/2007JPO3671.1.

Cetina-Heredia, P., M. Roughan, E. van Sebille, S. Keating, and G. B. Brassington, 2019: Retention and leakage of water by mesoscale eddies in the East Australian current system. *J. Geophys. Res. Oceans*, **124**, 2485–2500, https://doi.org/10.1029/2018JC014482.

Chelton, D. B., M. G. Schlax, R. M. Samelson, and R. A. de Szoeke, 2007: Global observations of large oceanic eddies. *Geophys. Res. Lett.*, **34**, L15606, https://doi.org/10.1029/2007GL030812.

——, ——, and ——, 2011a: Global observations of nonlinear mesoscale eddies. *Prog. Oceanogr.*, **91**, 167–216, https://doi.org/10.1016/j.pocean.2011.01.002.

——, P. Gaube, M. G. Schlax, J. J. Early, and R. M. Samelson, 2011b: The influence of nonlinear mesoscale eddies on near-surface oceanic chlorophyll. *Science*, **334**, 328–332, https://doi.org/10.1126/science.1208897.

Choi, J., Y.-G. Park, W. Kim, and Y. H. Kim, 2019: Characterization of submesoscale turbulence in the East/Japan Sea using geostationary ocean color satellite images. *Geophys. Res. Lett.*, **46**, 8214–8223, https://doi.org/10.1029/2019GL083892.

D'Asaro, E. A., and Coauthors, 2018: Ocean convergence and the dispersion of flotsam. *Proc. Natl. Acad. Sci. USA*, **115**, 1162–1167, https://doi.org/10.1073/pnas.1718453115.

de Marez, C., T. Meunier, M. Morvan, P. L'Hégaret, and X. Carton, 2020: Study of the stability of a large realistic cyclonic eddy. *Ocean Modell.*, **146**, 101540, https://doi.org/10.1016/j.ocemod.2019.101540.

Delandmeter, P., and E. van Sebille, 2019: The parcels v2.0 Lagrangian framework: New field interpolation schemes. *Geosci. Model Dev.*, **12**, 3571–3584, https://doi.org/10.5194/gmd-12-3571-2019.

Dong, J., B. Fox-Kemper, H. Zhang, and C. Dong, 2021: The scale and activity of symmetric instability estimated from a global submesoscale-permitting ocean model. *J. Phys. Oceanogr.*, **51**, 1655–1670, https://doi.org/10.1175/JPO-D-20-0159.1.

——, ——, Z. Jing, Q. Yang, J. Tian, and C. Dong, 2022: Turbulent dissipation in the surface mixed layer of an anticyclonic mesoscale eddy in the South China Sea. *Geophys. Res. Lett.*, **49**, e2022GL100016, https://doi.org/10.1029/2022GL100016.

Ducet, N., P. Y. Le Traon, and G. Reverdin, 2000: Global high-resolution mapping of ocean circulation from TOPEX/Poseidon and ERS-1 and -2. *J. Geophys. Res.*, **105**, 19 477–19 498, https://doi.org/10.1029/2000JC900063.

Early, J. J., R. M. Samelson, and D. B. Chelton, 2011: The evolution and propagation of quasigeostrophic ocean eddies. *J. Phys. Oceanogr.*, **41**, 1535–1555, https://doi.org/10.1175/2011JPO4601.1.

Ferrari, R., and C. Wunsch, 2009: Ocean circulation kinetic energy: Reservoirs, sources, and sinks. *Annu. Rev. Fluid Mech.*, **41**, 253–282, https://doi.org/10.1146/annurev.fluid.40.111406.102139.

Fox-Kemper, B., R. Ferrari, and R. Hallberg, 2008: Parameterization of mixed layer eddies. Part I: Theory and diagnosis. *J. Phys. Oceanogr.*, **38**, 1145–1165, https://doi.org/10.1175/2007JPO3792.1.

Fu, L.-L., and C. Ubelmann, 2014: On the transition from profile altimeter to swath altimeter for observing global ocean surface topography. *J. Atmos. Oceanic Technol.*, **31**, 560–568, https://doi.org/10.1175/JTECH-D-13-00109.1.

Gula, J., M. J. Molemaker, and J. C. McWilliams, 2014: Submesoscale cold filaments in the Gulf Stream. *J. Phys. Oceanogr.*, **44**, 2617–2643, https://doi.org/10.1175/JPO-D-14-0029.1.

——, —— and ——, 2016: Topographic generation of submesoscale centrifugal instability and energy dissipation. *Nat. Commun.*, **7**, 12811, https://doi.org/10.1038/ncomms12811.

Hoskins, B. J., 1982: The mathematical theory of frontogenesis. *Annu. Rev. Fluid Mech.*, **14**, 131–151, https://doi.org/10.1146/annurev.fl.14.010182.001023.

Hsu, P.-C., C.-Y. Ho, H.-J. Lee, C.-Y. Lu, and C.-R. Ho, 2020: Temporal variation and spatial structure of the Kuroshio-induced submesoscale island vortices observed from GCOM-C and Himawari-8 data. *Remote Sens.*, **12**, 883, https://doi.org/10.3390/rs12050883.

Johnson, L., C. M. Lee, E. A. D'Asaro, L. Thomas, and A. Shcherbina, 2020: Restratification at a California Current upwelling front. Part I: Observations. *J. Phys. Oceanogr.*, **50**, 1455–1472, https://doi.org/10.1175/JPO-D-19-0203.1.

Klein, P., and G. Lapeyre, 2009: The oceanic vertical pump induced by mesoscale and submesoscale turbulence. *Annu. Rev. Mar. Sci.*, **1**, 351–375, https://doi.org/10.1146/annurev.marine.010908.163704.

Lange, M., and E. van Sebille, 2017: Parcels v0.9: Prototyping a Lagrangian ocean analysis framework for the petascale age. *Geosci. Model Dev.*, **10**, 4175–4186, https://doi.org/10.5194/gmd-10-4175-2017.

Lee, D.-K., and P. P. Niiler, 1998: The inertial chimney: The near-inertial energy drainage from the ocean surface to the deep layer. *J. Geophys. Res.*, **103**, 7579–7591, https://doi.org/10.1029/97JC03200.

Li, J., G. Wang, and X. Zhai, 2017: Observed cold filaments associated with mesoscale eddies in the South China Sea. *J. Geophys. Res. Oceans*, **122**, 762–770, https://doi.org/10.1002/2016JC012353.

Liang, X. S., 2016: Canonical transfer and multiscale energetics for primitive and quasigeostrophic atmospheres. *J. Atmos. Sci.*, **73**, 4439–4468, https://doi.org/10.1175/JAS-D-16-0131.1

Lin, H., Z. Liu, J. Hu, D. Menemenlis, and Y. Huang, 2020: Characterizing meso- to submesoscale features in the South China Sea. *Prog. Oceanogr.*, **188**, 102420, https://doi.org/10.1016/j.pocean.2020.102420.

——, S. Xu, Z. Liu, J. Hu, F. Zhang, and Z. Cao, 2023: Scale-dependent temperature-salinity compensation in frontal regions of the Taiwan Strait. *J. Geophys. Res. Oceans*, **128**, e2022JC019134, https://doi.org/10.1029/2022JC019134.

Liu, T., R. Abernathey, A. Sinha, and D. Chen, 2019: Quantifying Eulerian eddy leakiness in an idealized model. *J. Geophys. Res. Oceans*, **124**, 8869–8886, https://doi.org/10.1029/2019JC015576.

Mahadevan, A., 2016: The impact of submesoscale physics on primary productivity of plankton. *Annu. Rev. Mar. Sci.*, **8**, 161–184, https://doi.org/10.1146/annurev-marine-010814-015912.

Mason, E., A. Pascual, and J. C. McWilliams, 2014: A new sea surface height–based code for oceanic mesoscale eddy tracking. *J. Atmos. Oceanic Technol.*, **31**, 1181–1188, https://doi.org/10.1175/JTECH-D-14-00019.1.

McGillicuddy, D. J., Jr., and Coauthors, 1998: Influence of mesoscale eddies on new production in the Sargasso Sea. *Nature*, **394**, 263–266, https://doi.org/10.1038/28367.

McWilliams, J. C., 2016: Submesoscale currents in the ocean. *Proc. Roy. Soc.*, **472A**, 20160117, https://doi.org/10.1098/rspa.2016.0117.

——, F. Colas, and M. J. Molemaker, 2009: Cold filamentary intensification and oceanic surface convergence lines. *Geophys. Res. Lett.*, **36**, L18602, https://doi.org/10.1029/2009GL039402.

Meng, Y., H. Liu, R. Ding, P. Lin, M. Ding, and P. Wang, 2021: The predictability limit of ocean mesoscale eddy tracks in the Kuroshio Extension region. *Front. Mar. Sci.*, **8**, 658125, https://doi.org/10.3389/fmars.2021.658125.

Peng, J.-P., P. Holtermann, and L. Umlauf, 2020: Frontal instability and energy dissipation in a submesoscale upwelling filament. *J. Phys. Oceanogr.*, **50**, 2017–2035, https://doi.org/10.1175/JPO-D-19-0270.1.

——, J. Dräger-Dietel, R. P. North, and L. Umlauf, 2021: Diurnal variability of frontal dynamics, instability, and turbulence in a submesoscale upwelling filament. *J. Phys. Oceanogr.*, **51**, 2825–2843, https://doi.org/10.1175/JPO-D-21-0033.1.

Qiu, B., 1999: Seasonal eddy field modulation of the North Pacific subtropical countercurrent: TOPEX/Poseidon observations and theory. *J. Phys. Oceanogr.*, **29**, 2471–2486, https://doi.org/10.1175/1520-0485(1999)029<2471:SEFMOT>2.0.CO;2.

——, S. Chen, P. Klein, J. Wang, H. Torres, L.-L. Fu, and D. Menemenlis, 2018: Seasonality in transition scale from balanced to unbalanced motions in the world ocean. *J. Phys. Oceanogr.*, **48**, 591–605, https://doi.org/10.1175/JPO-D-17-0169.1.

Schubert, R., J. Gula, R. J. Greatbatch, B. Baschek, and A. Biastoch, 2020: The submesoscale kinetic energy cascade: Mesoscale absorption of submesoscale mixed layer eddies and frontal downscale fluxes. *J. Phys. Oceanogr.*, **50**, 2573–2589, https://doi.org/10.1175/JPO-D-19-0311.1.

Shi, Q., and G. Wang, 2020: Observed warm filaments from the Kuroshio associated with mesoscale eddies. *Remote Sens.*, **12**, 3090, https://doi.org/10.3390/rs12183090.

Sinha, A., D. Balwada, N. Tarshish, and R. Abernathey, 2019: Modulation of lateral transport by submesoscale flows and inertia-gravity waves. *J. Adv. Model. Earth Syst.*, **11**, 1039–1065, https://doi.org/10.1029/2018MS001508.

Sullivan, P. P., and J. C. McWilliams, 2017: Frontogenesis and frontal arrest of a dense filament in the oceanic surface boundary layer. *J. Fluid Mech.*, **837**, 341–380, https://doi.org/10.1017/jfm.2017.833.

Taylor, J. R., and R. Ferrari, 2010: Buoyancy and wind-driven convection at mixed layer density fronts. *J. Phys. Oceanogr.*, **40**, 1222–1242, https://doi.org/10.1175/2010JPO4365.1.

Thomas, L. N., J. R. Taylor, R. Ferrari, and T. M. Joyce, 2013: Symmetric instability in the Gulf Stream. *Deep-Sea Res. II*, **91**, 96–110, https://doi.org/10.1016/j.dsr2.2013.02.025.

von Appen, W.-J., C. Wekerle, L. Hehemann, V. Schourup-Kristensen, C. Konrad, and M. H. Iversen, 2018: Observations of a submesoscale cyclonic filament in the marginal ice zone. *Geophys. Res. Lett.*, **45**, 6141–6149, https://doi.org/10.1029/2018GL077897.

Wang, C., Z. Liu, and H. Lin, 2022: Interpreting consequences of inadequate sampling of oceanic motions. *Limnol. Oceanogr. Lett.*, **7**, 385–391, https://doi.org/10.1002/lol2.10260.

——, ——, and ——, 2023: On dynamical decomposition of multiscale oceanic motions. *J. Adv. Model. Earth Syst.*, **15**, e2022MS003556, https://doi.org/10.1029/2022MS003556.

Wang, Y., M. J. Olascoaga, and F. J. Beron-Vera, 2015: Coherent water transport across the South Atlantic. *Geophys. Res. Lett.*, **42**, 4072–4079, https://doi.org/10.1002/2015GL064089.

Wunsch, C., and R. Ferrari, 2004: Vertical mixing, energy, and the general circulation of the oceans. *Annu. Rev. Fluid Mech.*, **36**, 281–314, https://doi.org/10.1146/annurev.fluid.36.050802.122121.

Yang, Q., W. Zhao, X. Liang, J. Dong, and J. Tian, 2017: Elevated mixing in the periphery of mesoscale eddies in the South China Sea. *J. Phys. Oceanogr.*, **47**, 895–907, https://doi.org/10.1175/JPO-D-16-0256.1.

Zhang, W. G., and G. G. Gawarkiewicz, 2015: Dynamics of the direct intrusion of Gulf Stream ring water onto the Mid-Atlantic bight shelf. *Geophys. Res. Lett.*, **42**, 7687–7695, https://doi.org/10.1002/2015GL065530.

Zhang, Z., W. Wang, and B. Qiu, 2014: Oceanic mass transport by mesoscale eddies. *Science*, **345**, 322–324, https://doi.org/10.1126/science.1252418.

Zheng, R., and Z. Jing, 2022: Submesoscale-enhanced filaments and frontogenetic mechanism within mesoscale eddies of the South China Sea. *Acta Oceanol. Sin.*, **41**, 42–53, https://doi.org/10.1007/s13131-021-1971-3.

Zhong, Y., A. Bracco, J. Tian, J. Dong, W. Zhao, and Z. Zhang, 2017: Observed and simulated submesoscale vertical pump of an anticyclonic eddy in the South China Sea. *Sci. Rep.*, **7**, 44011, https://doi.org/10.1038/srep44011.